

Space charge potential of proton conducting $BaCe_{0.8}Y_{0.2}O_{2.9-\delta}$

S.-J. Song^{a,*}, J.-H. Moon^a, T. H. Lee^b, S. E. Dorris^b and U. Balachandran^b

^aSchool of Materials Science and Engineering Chonnam National University 300 Yongbong-dong, Buk-gu, Gwangju 500-757, Korea

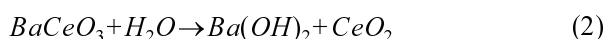
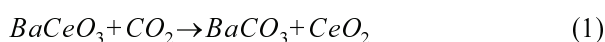
^bEnergy System Division Argonne National Laboratory Argonne, IL 60439, USA

Proton conducting $BaCe_{0.8}Y_{0.2}O_{2.9-\delta}$ (BCY) was prepared by solid-state sintering at various elevated temperatures (1623-1873 K) to control its microstructure and defect chemistry at the grain boundaries. The bulk and grain boundary conductivity were measured over the temperature range of 373-1173 K under 4% H_2 /balanced by He ($p_{H_2O} = 0.03$ atm) by an AC impedance analyzer (Solatron 1260). For the ternary BCY system, the predominant configuration of majority defect pairs was described as functions of pO_2 , a_{BaO} , and temperature and a space charge potential theory was developed. It was shown by TEM that the grain boundaries of the sintered disks were free of any second phase. The depletion of effectively positively charged protons with a positive space charge potential with respect to the bulk ($\phi_a = 0$) was explained by negatively charged yttrium enrichment across the grain boundaries. The bulk conductivity was around two orders of magnitude higher than the grain boundary conductivity.

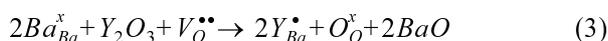
Key words: Proton conductor, $BaCe_{0.8}Y_{0.2}O_{2.9-\delta}$, Space charge potential.

Introduction

During the last decade, acceptor doped barium cerate has been intensively investigated because of its potential applications for fuel cells, sensors, membranes, and steam electrolyzers [1-4]. However, although it has good proton conducting properties, barium cerate has not been able to be used in electrochemical devices because of its thermodynamic and long-term kinetic instability, especially in the presence of CO , CO_2 , and water [5, 6] due to the following proposed-decomposition reactions:



Its thermal stability has also been brought into question by the fact that a significant vapor pressure of barium cerate was measured by mass spectrometry above 1774 K and $BaO(g)$ was identified as being the main gaseous species [7]. Atomistic simulation results [8, 9] show that the formation of Ba and O vacancy pairs is the most energetically favorable point defect, resulting in the loss of BaO and formation of CeO_2 at very high temperature. The loss of BaO from yttrium doped barium cerate (BCY) was explained by either the dopant redistribution over the A and B sites or by the evaporation of BaO as described below [10]:



In contrast, recently, the thermal instability of acceptor doped barium cerate was made use of to produce a single material functioning as both an anode and an electrolyte for solid oxide fuel cells, by intentionally vaporizing BaO from doped barium cerate, producing an electron-conducting Ce-rich phase [11].

All of these phenomena lead us to infer that the thermal and chemical stability of BCY may change not only its bulk defect structure but also its grain boundary chemistry. The grain-boundary conduction consists of contributions from the grain boundary interfaces and the space charge layers, which are structurally a part of the bulk, but electrically belong to the grain boundary [12, 13]. Therefore, the thermal history including the sintering temperature of the BCY samples and the difference in size between the ionic dopant and host cations may affect the space charge potential and thickness, because the origin of the space charge is generally ascribed to the difference in the free energy of formation of the vacancies and interstitials in the case of Frenkel disorder or of the individual vacancies in the case of Schottky disorder, as well as the elastic strain energy developed by dopant substitution [14].

This paper begins by reporting the equilibrium defect diagram for ternary BCY as a function of the BaO activity and oxygen partial pressure at a fixed temperature. The dependence of the sintering temperature on both the bulk/grain-boundary composition and the bulk/grain-boundary conductivity was studied. The grain boundary conductivity will be discussed in terms of the space charge potential.

*Corresponding author:

Tel : 82-62-530-1706

Fax: 82-62-530-1699

E-mail: song@chonnam.ac.kr

Theory

Defect structure

For the ternary BCY system, because the BaO vapor pressure is not negligible at elevated sintering temperatures, cation nonstoichiometry should be considered. Recent molecular dynamic calculation studies on the BCY defect structure [15, 16] also showed that the most favorable defect formation energy was for Ba and O vacancy pairs, which might result in the loss of BaO at very high temperatures. Therefore, when their defect-related material properties are described, we need three thermodynamic parameters to calculate the equilibrium defect concentration: T and pO_2 (oxygen partial pressure), together with a_{BaO} (activity of BaO) defining the barium vacancy concentration under the sintering conditions. In addition, to define the proton concentration under the given thermodynamic conditions, the proton incorporation reaction should also be considered.

The defect notation of Kroger and Vink [15] is used, in which the subscripts indicate the site, while the superscripts (x), (\bullet), and (\prime) indicate zero, positive, and negative effective charges, respectively. Mass action laws are applied to defect equilibria as follows.

Internal equilibria:

$$null = V_{Ba}^{\prime\prime} + V_{Ce}^{\prime\prime\prime} + 3V_O^{\bullet\bullet}; K_s = [V_{Ba}^{\prime\prime}][V_{Ce}^{\prime\prime\prime}][V_O^{\bullet\bullet}]^3 \quad (5)$$

where K_s is the equilibrium constant for Schottky-Wagner disorder:

$$null = e^{\prime} + h^{\bullet}; K_i = n \cdot p \quad (6)$$

where K_i is the equilibrium constant for the electron-hole pair intrinsic reaction.

External equilibria:

$$O_O^x \rightarrow \frac{1}{2}O_2(g) + V_O^{\bullet\bullet} + 2e^{\prime}; K_R = [V_O^{\bullet\bullet}]n^2 p_{O_2}^{1/2} \quad (7)$$

where K_R is the equilibrium constant for the exchange of oxygen:

$$H_2O(g) + V_O^{\bullet\bullet} + O_O^x \rightarrow 2OH_O^{\bullet}; K_W = \frac{[OH_O^{\bullet}]^2}{[V_O^{\bullet\bullet}]P_{H_2O}} \quad (8)$$

where K_W is the equilibrium constant for the exchange of water.

Vaporization equilibrium of BaO:

$$Ba_{Ba}^x + Ce_{Ce}^x + 3O_O^x \rightarrow V_{Ba}^{\prime\prime} + Ce_{Ce}^x + V_O^{\bullet\bullet} + 2O_O^x + BaO(g); K_B = [V_{Ba}^{\prime\prime}][V_O^{\bullet\bullet}]a_{BaO} \quad (9)$$

where K_B is the equilibrium constant for the vaporization of BaO, and a_{BaO} is the activity of BaO.

Charge neutrality condition:

$$n + 2[V_{Ba}^{\prime\prime}] + 4[V_{Ti}^{\prime\prime\prime}] + [Y_{Ce}^{\prime}] = p + 2[V_O^{\bullet\bullet}] + [OH_O^{\bullet}] \quad (10)$$

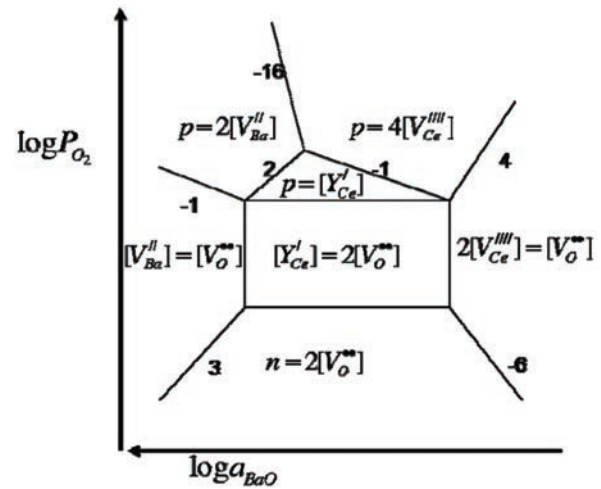


Fig. 1. Predominant defect equilibrium diagram as functions of $\log pO_2$ and a_{BaO} at a given temperature for $BaCe_{0.8}Y_{0.2}O_{3-\delta}$ under dry condition. Under wet conditions, protons may be the major positive defects instead of oxygen vacancies.

The possibility of Frenkel disorder is ruled out because, according to the atomistic simulation, the perovskite structure is highly unlikely to accommodate ion interstitials [15, 16].

In the case of the heavily doped ternary system, the predominant configuration of majority defect pairs [16] should be described as functions of pO_2 , a_{BaO} , and temperature because the full description of the ternary system's properties needs to specify three degree of freedom. Figure 1 shows the defect equilibrium diagram as functions of pO_2 , and a_{BaO} with a fixed temperature at a low water vapor pressure ($p_{H_2O} = 10^{-6}$). Then, all the ionic and electronic defect concentrations may be calculated as functions of pO_2 , and a_{BaO} at a given temperature within a regime characterized by simplified charge neutrality conditions by solving Eqs. (4)-(6). At higher water vapor pressure ($p_{H_2O} \gg 10^{-2}$), the oxygen vacancies may be filled with hydroxyl ions and the corresponding new charge neutrality conditions are also given in Fig. 1. The border line between the two regimes characterized by simplified charge neutrality was calculated by considering the continuity equation.

For larger defect concentrations at low temperature, we may expect defects to begin to interact. These interactions can be coulombic or mechanical and be attractive or repulsive. These interactions may change the activity coefficients and formation enthalpies of the defects, and may lead to associations between defects which attract each other. However, defect association is beyond the scope of this study.

Space charge potential

In the case of the ionic compounds, the composition at the surface/interface may differ from that in the bulk, resulting in a difference in electrical potential between the grain boundary and bulk. Due to the presence of excess ions at the grain boundaries under equilibrium, a space charge potential is developed to compensate for

these excess charges [17].

Under thermodynamic equilibrium, the electrochemical potential for oxygen vacancies is constant throughout the system:

$$\eta_{V_{O}^{\bullet\bullet}} = \eta_{V_{O}^{\bullet\bullet},x} = \eta_{V_{O}^{\bullet\bullet},\infty} \quad (11)$$

where x is the position in the direction perpendicular to the grain boundary with $x = 0$ at the interface and $x = \infty$ inside the bulk. The equilibrium oxygen vacancy concentration may be obtained by combining the chemical potential (μ) of oxygen vacancies and the electrical potential (ϕ) assuming $\phi_{\infty} = 0$ (bulk potential):

$$[V_{O}^{\bullet\bullet}]_x = [V_{O}^{\bullet\bullet}]_{\infty} \exp(-2q\phi_x/kT) \quad (12)$$

It is assumed that the grain is large with respect to the width of the space-charge layer and also large enough for the enrichment or depletion of oxygen vacancies to the grain boundary layer not to appreciably deplete the bulk oxygen vacancy concentration. The spatially varying electrical static potential, $\phi(x)$, is governed by Poisson's equation:

$$\frac{d^2\phi}{dx^2} = -\frac{4\pi}{\epsilon} \rho(x) \quad (13)$$

where ϵ is the dielectric constant, and $\rho(x)$ is the charge density, given by $\rho(x) = (2[V_{O}^{\bullet\bullet}]_x - [Y_{Ce}']_x)q$. The solution of Poisson's equation for acceptor-doped alumina was given in ref. 18. In this study, we focus on determining the sign and magnitude of the space charge potential rather than solving Eq. (13). The electrical static potential, $\phi(x)$, may be obtained from Eq. (12), as follows:

$$q\phi_x = \frac{kT}{2} \ln \frac{[V_{O}^{\bullet\bullet}]_{\infty}}{[V_{O}^{\bullet\bullet}]_x} \quad (14)$$

where $\phi(x)$ has a positive potential with respect to the bulk ($\phi_{\infty} = 0$) when $[V_{O}^{\bullet\bullet}]_x < [V_{O}^{\bullet\bullet}]_{\infty}$, which corresponds to Y_{Ce}' segregation and $V_{O}^{\bullet\bullet}$ depletion. Y_{Ce}' may be depleted and $V_{O}^{\bullet\bullet}$ segregated when $[V_{O}^{\bullet\bullet}]_x > [V_{O}^{\bullet\bullet}]_{\infty}$, resulting in a negative space charge potential with respect to the bulk.

In the case of a high water vapor pressure ($p_{H_2O} > 10^{-2}$), the charge neutrality condition of the bulk is given by:

$$[Y_{Ce}']_{\infty} = [OH_{O}^{\bullet}]_{\infty} \quad (15)$$

The equilibrium proton concentration may be obtained as follows:

$$[OH_{O}^{\bullet}]_x = [Y_{Ce}']_{\infty} \exp(-q\phi_x/kT) \quad (16)$$

The electrical static potential may be expressed as follows:

$$q\phi_x = kT \ln \frac{[Y_{Ce}']_{\infty}}{[OH_{O}^{\bullet}]_x} \quad (17)$$

When OH_{O}^{\bullet} enrichment occurs at the space charge layer, $\phi(x)$ has a negative potential with respect to the bulk ($\phi_{\infty} = 0$) with $[OH_{O}^{\bullet}]_x > [Y_{Ce}']_{\infty} (=2[V_{O}^{\bullet\bullet}]_{\infty})$, and vice versa.

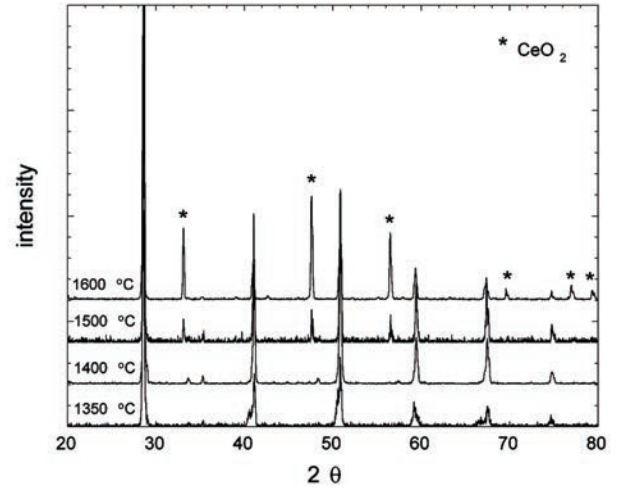


Fig. 2. XRD patterns of $BaCe_{0.8}Y_{0.2}O_{3-\delta}$ sintered at various temperatures.

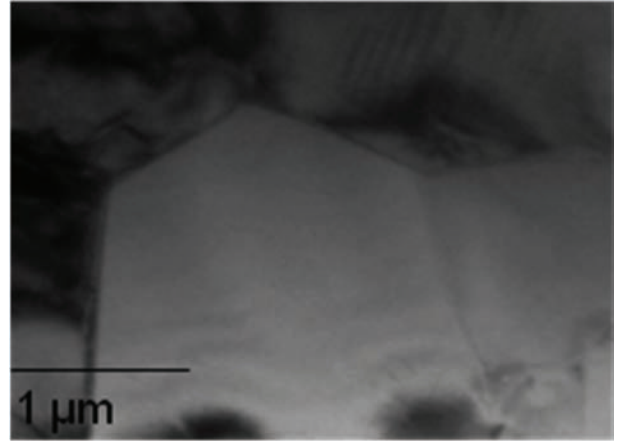


Fig. 3. TEM images for a triple grain boundary junction of $BaCe_{0.8}Y_{0.2}O_{3-\delta}$ sintered at 1673 K.

Experiments

BCY powders (purchased from Praxair) were pressed into pellets, and sintered at various temperatures, in the range of 1623-1873 K for 10 h in 4% H_2 balanced by He. The X-ray diffraction spectra from the surface of specimens was shown in Fig. 2. X-ray diffraction spectra for the as-sintered surface confirmed the presence of a single phase with an orthorhombic perovskite structure for the sample sintered at 1623 K. For the other samples sintered at temperature above 1673 K, a second phase (CeO_2) was found as expected from the observation of Ba evaporation. After mechanically polishing the samples, their microstructures were investigated by SEM, and TEM. A typical TEM image of BCY is shown in Fig. 3. The grain boundaries of the sintered disks were free of second phase as indicated by the absence of significant segregation.

The chemical composition at the grain/grain-boundary was also studied by EDX. The mole ratio of $(Ce+Y)/Ba$ was 0.98 for the polished samples sintered at both 1673 K and 1873 K showing that the evaporation of Ba

did not change the cation nonstoichiometry for the bulk composition. However, across the boundary, the EDX results showed a slight increase in the yttrium content.

For the electrical measurements, the pellets were coated with Pt paste (Engelhard 6926) and heated at 1273 K for 1 h. The conductivity was measured with an impedance analyzer (Solatron 1260) over the frequency range of 0.1 to 1 MHz with an amplitude of 100 mV and in the temperature range of 323 K to 1173 K under 4% H_2 balanced by He ($p_{H_2O} = 0.03$ atm).

Results and Discussions

The electrical response of the BCY samples below 573 K typically showed three semicircles in the Nyquist plot: one at high frequencies, corresponding to the bulk characteristics; one at medium frequencies, related to the grain boundary resistance, and one at low frequencies, associated with the electrode response. The bulk conductivity was calculated by multiplying the inverse bulk resistance ($1/R_b$) by L/A , where A is the cross sectional area, and L is the thickness of the sample. In order to calculate the grain and grain boundary resistivity from the impedance measurements, we need macroscopic and microscopic information about the sample. A method of extracting the resistivity was reported, in which the capacitances of the bulk and grain are compared without the need for further microscopic information, assuming that the bulk and grain boundary dielectric constants are approximately equal [19, 20]. The specific grain boundary conductivity can be calculated from:

$$\sigma_{g,b} = \frac{L}{R_{g,b}} \frac{\delta_{g,b}}{d_g} \quad (18)$$

where $R_{g,b}$ is the grain boundary resistance, d_g is the grain size, and $\delta_{g,b}$ is the grain boundary thickness (mainly the thickness of the space charge layer). $\delta_{g,b}$ may also be calculated from the ratios of the bulk and grain boundary capacitances:

$$\delta_{g,b} = \frac{\epsilon_{g,b}}{\epsilon_b} \frac{C_b}{C_{g,b}} d_{g,b} \approx \frac{C_b}{C_{g,b}} d_{g,b} \quad (19)$$

if we approximate the dielectric constant of the grain boundary ($\epsilon_{g,b}$) to the bulk value (ϵ_b). A detailed mathematical explanation was given in Ref. 19. Assuming an equivalent circuit of three parallel RC circuits connected in series, the impedance diagrams were fitted to obtain the resistance, characteristic frequency, and capacitance of the bulk, grain boundary, and electrodes.

Arrhenius plots of the electrical conductivity are shown in Fig. 4. The bulk conductivity was around two orders of magnitude higher than the grain boundary conductivity over the temperature range of 373-573 K in a feed gas consisting of 4% H_2 /balance He ($p_{H_2O} = 0.03$ atm). This finding suggests that the grain boundary may not provide a pathway for fast proton transport, and that bulk transport makes the major contribution to the total conductivity.

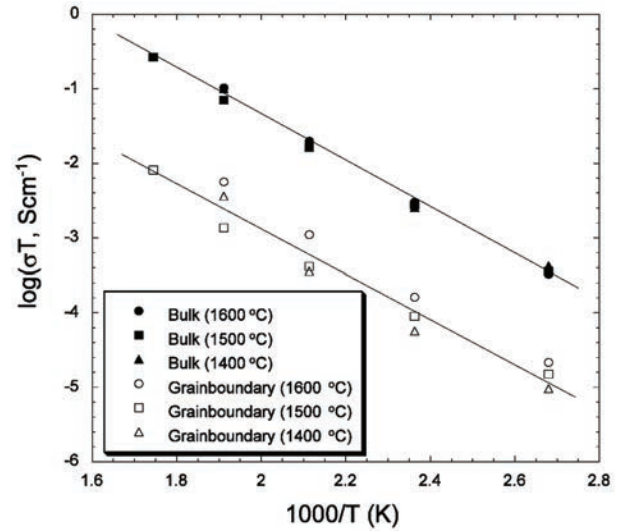


Fig. 4. Arrhenius plots of bulk and grain boundary conductivity for $BaCe_{0.8}Y_{0.2}O_{3-\delta}$ sintered at various temperatures.

The calculated activation energy, consisting of the formation and migration energy for mobile defect species, is 0.6 eV for both bulk and grain boundary conduction. In the case where the grain boundary activation energy is much higher than that of bulk conduction, it may be fair to say that the intergranular second phase plays a role in blocking the charge transport. However, a negligible difference in activation energy was observed for the BCY samples. The results also showed that the activation energy of grain boundary conduction was insensitive to the final sintering temperature. Because the grain boundaries of the sintered disks were free of second phase as shown in Fig. 3, the high resistive grain boundary conduction may originate from both the grain-to-grain contacts and space charge.

In addition, the EDX results showed a slight yttrium enrichment (effectively negatively charged defects in BCY) across the grain boundaries. Because the grain boundary interface (core) is clean as shown in Fig. 3, the yttrium enrichment across the grain boundaries can be ascribed to the existence of space charge layers. When trivalent yttrium dopant substitutes for cerium, it may affect the concentration of intrinsic defects and influence their redistribution by adjusting their concentration in the space charge region in the field created by the native defects, because the elastic strain energy may be negligible, due to the similar ionic radii of cerium and yttrium at the octahedral sites [17]. Effectively negatively charged yttrium enrichment at the space charge layer corresponds to the depletion of effectively positively charged defects with a positive space charge potential with respect to the bulk ($\phi_{sc} = 0$). Because protons rather than oxygen vacancies are known as the major positively charged defects within the experimental conditions, proton depletion along with yttrium enrichment may occur at the space charge layer, as shown in Eq. 17. The smaller grain boundary conductivity results from the property of the space charge layer,

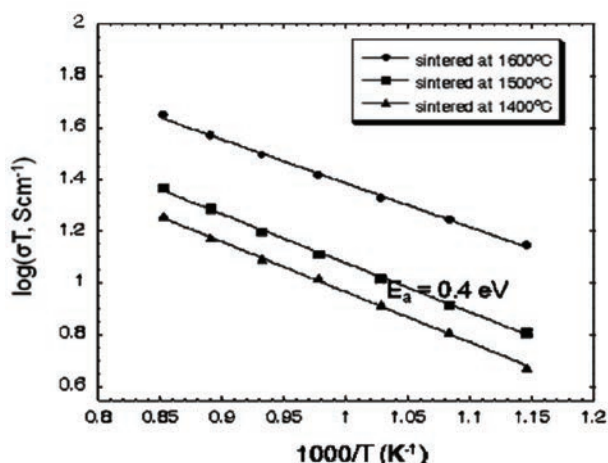


Fig. 5. Temperature dependence of total electrical conductivity for $\text{BaCe}_{0.8}\text{Y}_{0.2}\text{O}_{3-\delta}$ sintered at various temperatures.

originating from the depletion of positively charged protons due to the positively charged interface core, as explained above.

Above 600 °C, both the bulk and grain boundary responses are incorporated into the high-frequency offset, leaving the electrode response as the only clearly defined semicircle [21]. Figure 5 shows the Arrhenius plots of the temperature dependence of total conductivity of BCY in 4% H_2 ($p_{\text{H}_2\text{O}} = 0.03$ atm) feed gas at 773–1173 K. The calculated activation energy is ≈ 0.4 eV, which is a typical value for proton-conducting oxides [22]. The change of the crystal structure with temperature under wet conditions [23], which was reported in neutron diffraction studies, is the cause of the variation in activation energy with temperature. The higher total conductivity of the sample sintered at 1873 K may also be explained by the difference in the grain size and boundaries.

Conclusions

The BCY disks were sintered at various elevated temperatures to control their microstructure and chemistry at the grain boundaries. The X-ray diffraction spectra confirm the formation of CeO_2 phase at the surface of the sintered BCY at temperatures above 1673 K. It was shown by TEM that the grain boundaries of the sintered disks were free of second phase. The EDX results confirmed that effectively negatively charged yttrium was enriched across the grain boundaries, corresponding to the depletion of effectively positive charged protons, with positive space charge potential with respect to the bulk ($\phi_\infty = 0$).

The bulk conductivity was around two orders of magnitude higher than the grain boundary conductivity over the temperature range of 373–573 K in a feed gas consisting of 4% H_2 /balanced by He ($p_{\text{H}_2\text{O}} = 0.03$ atm).

Acknowledgment

This work was supported by a Korea Research Foundation Grant funded by the Korean Government (MOEHRD, Basic Research Promotion Fund) (KRF-2007-331-D00199).

References

1. H. Iwahara, Y. Asakura, K. Katahira and M. Tanaka, *Solid State Ionics* 168 (2004) 299-310.
2. W.G Coors, *J. Electrochem. Soc.* 151[7] (2004) A994-A997.
3. K.D. Kreuer, *Solid State Ionics* 125 (1999) 285-302.
4. S.-J. Song, E.D. Wachsman, J. Rhodes, H.-S. Yoon, G. Zhang, K.-H. Lee, S.E. Dorris and U. Balachandran, *J. Mater. Sci.* 40 (2005) 4061-4066.
5. K.-H. Ryu and S. Haile, *Solid State Ionics* 125 (1999) 355-367.
6. K.D. Kreuer, *Solid State Ionics* 97 (1997) 1-15.
7. J. Wu, L.P. Li, W.T.P. Espinosa and S.M. Haile, *J. Mater. Res.* 19[8] (2004) 2366-2376.
8. J. Wu, R.A. Davies, M.S. Islam and S.M. Haile, *Chem. Mater.* 17 (2005) 846-851.
9. R. Glockner, M.S. Islam and T. Norby, *Solid State Ionics* 122 (1999) 145-156.
10. S.M. Haile, G. Staneff and K.-H. Ryu, *J. Mater. Sci.* 36 (2001) 1149-1160.
11. A. Tomita, T. Hibbino and M. Sano, *Electrochem. and Solid State Letters.* 8[7] (2005) A333-A336.
12. J. Maier, *Ber. Bunsenges. Phys. Chem.* 90 (1986) 26-33.
13. X. Guo and Y. Ding, *J. Electrochem. Soc.* 151[1] (2004) J1-J7.
14. R.B. Poeppel and J.M. Blakely, *Surf. Sci.* 15 (1969) 507-523.
15. F.A. Kroger and V.J. Vink, in D. Turnbull (Eds.), *Relations Between the Concentrations of Imperfections in Crystalline Solids*, *Solid State Physics*, Vol. 3, Academic Press, New York (1956) 307-435.
16. J.-Y. Kim, C.-R. Song and H.-I. Yoo, *J. Electroceram.* 1 : 1 (1997) 27-39.
17. J. Maier, *J. Eur. Ceram. Soc.* 24 (2004) 1251-1257.
18. S.K. Tiku and F.A. Kroger, *J. Amer. Ceram. Soc.* 63 (1980) 183-189.
19. S.M. Haile, D.L. West and J. Campbell, *J. Mater. Res.* 13 (1998) 1576-1596.
20. J.R. Macdonald, in *Impedance Spectroscopy*, J. Wiley & Sons, New York (1987).
21. S.-J. Song, T.-H. Lee, S.E. Dorris and U. Balachandran, *Mater. Chem. and Phys.* Submitted.
22. N. Bonanos, *Solid State Ionics* 53-56 (1992) 967-974.
23. K. S. Knight, *Solid State Ionics* 145 (2001) 275-294.